Original Research

Revista Brasileira de Física Médica (2026) 20:874

Computational Modeling of CyberKnife® System Using the Monte Carlo Method

Aline A.C. Granja[1,2], Paula C.G. Antunes[2], Gabriela R.S. Jesus[3], Pedro H.B. Cardoso[3], Julian M.B. Shorto[1]

[1]Institute for Energy and Nuclear Research, University of São Paulo, São Paulo, Brazil
[2]Albert Einstein School of Health Sciences, Albert Einstein Hospital, São Paulo, Brazil
[3] Hospital Vila Nova Star, Department of Radiotherapy, Oncologia D'Or, São Paulo, SP, Brazil

Abstract

The accuracy required in small-field dosimetry for stereotactic radiosurgery imposes limitations on the conventional dosimetric calibration protocols used in radiotherapy. This study presents the development and validation of a computational model of the CyberKnife® system using the Monte Carlo method with the MCNP6 code. The main objective is to establish a validated computational model that enables future research and clinical applications in stereotactic radiosurgery. The model was developed to validate the 60 mm conical collimator, and the results were compared with experimental data from percentage depth dose (PDD) and lateral dose profile (LDP) curves at depths of 10 cm and 20 cm. The analyses revealed the influence of field size and photon-source characteristics on the dose distribution, with good agreement between simulated and measured data within the established tolerance limits. These findings demonstrate that the proposed model accurately reproduces the CyberKnife® beam behavior and serves as a robust and promising tool for investigating treatment variables, supporting therapeutic planning, and optimizing stereotactic radiosurgery protocols.

Keywords: CyberKnife; Computational Simulation; Monte Carlo; MCNP; Small Fields.

1. Introduction

The need to improve dose delivery in radiotherapy has driven the development of more precise and minimally invasive technologies for the treatment of tumors and lesions. In this context, stereotactic radiosurgery (SRS) using small fields has gained prominence due to its ability to administer high radiation doses to confined target areas, while minimizing exposure to surrounding tissues (1, 2).

SRS was conceived in the 1940s and 1950s by neurosurgeon Lars Leksell, who developed the stereotactic frame to enable minimally invasive, high-precision treatment of deep intracranial lesions (3). The evolution of this technique subsequently led to the development of the robotic CyberKnife® system radiosurgery system, which eliminated the need for rigid immobilization structures, such as the stereotactic frame, by incorporating an X-ray image-guided tracking system (4).

The CyberKnife® system integrates a 6 MV photon linear accelerator (X-band Linac) with a flattening filter-free (FFF) design and a robotic arm offering six degrees of freedom. Its real-time tracking capability accounts for patient movements, such as respiration, enabling highly focused radiation delivery and enhancing treatment efficacy while reducing side effects. This precision makes the system particularly effective for lesions in hard-to-reach locations, with clinical applications including tumors, arteriovenous malformations, and functional disorders of the central nervous system. Furthermore, as a non-invasive treatment, it allows patients to quickly resume their daily activities (5).

The technique also enables hypofractionated treatment regimens, where higher doses are delivered in fewer sessions. For example, a study by Fransson et al. (2021) (6) demonstrated the effectiveness of an ultrahypofractionated regimen for prostate cancer, delivering 42.7 Gy in seven sessions compared with the conventional protocol of 78 Gy in 39 sessions, achieving equivalent results with greater patient convenience (7).

However, despite its advantages, the use of small fields with the CyberKnife® system presents significant dosimetric challenges. Under these conditions, limitations arise, such as lateral electronic disequilibrium, partial occlusion of the primary source, and measurement difficulties due to detector size. These factors compromise the direct application of standardized dosimetry protocols, which were developed for conventional reference fields of 10 × 10 cm² at a source-to-surface (SSD) of 100 cm (7). Consequently, the observed effects include a reduction in central dose, penumbra overlap, and interference with the measured signal (8).

To overcome these challenges, the Monte Carlo method (MC) has been widely recommended due to its high accuracy in simulating particle transport and energy deposition in heterogeneous media (9). This study proposes the development and validation of a computational model of the CyberKnife® system using the MCNP6 (Monte Carlo N-Particle, version 6.2) code, based on dosimetric data. The model aims to serve as a tool for dosimetric analysis and clinical support in small-field stereotactic radiosurgery.

2. Materials and Methods

2.1. Cyberknife® Head

The head of the CyberKnife® system is responsible for generating and controlling the 6 MV photon treatment beam, operating in flattening filter-free (FFF) mode, *i.e.*, without a flattening filter. The head

structure is divided into two parts: a fixed upper section and a removable lower section. Figure 1 shows a schematic of the head (5, 10).

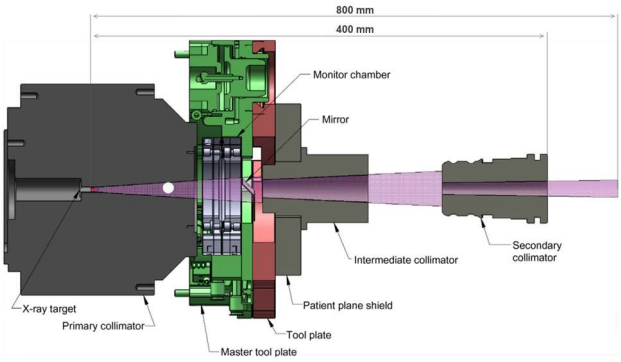

Figure 1. Schematic of the CyberKnife® Head (not to scale). The source-to-output distance is 400 mm, and the source-to-isocenter distance is 800 mm, where the field sizes are defined (5).

The upper part houses the linear accelerator (LINAC), which generates the treatment beam by accelerating electrons in a vacuum tube and colliding them against a tungsten target. The output is a 6 MV X-ray beam with a dose rate of up to 1000 cGy/min. In this region, the primary collimator (PC), made of tungsten, defines the maximum field of 115 × 100 mm, along with a dose-monitoring chamber and a laser system for calibration.

The lower part contains the secondary collimation system, composed of an intermediate collimator (IC) and a secondary collimator (SC), both made of tungsten. The SC can be mechanically exchanged by a robotic arm, with three types available:

- Fixed cones: diameters ranging from 5 mm to 60 mm (Figure 2);
- Iris™: variable aperture with dodecagonal geometry, replicating the same diameters as the cones;
- InCise2™ MLC: multileaf collimator system with a maximum opening of 115 × 100 mm.

Figure 2. Cones comprising the secondary collimation system (11).

In this study, conical collimators were used for their beam sharpness and suitability for small-volume targets.

2.2. Clinical Commissioning

Clinical measurements were performed using a SunSCAN 3D water tank (Sun Nuclear Corporation) with 40 cm depth and 65 cm diameter (12). The commissioning process was divided into three stages:

1. Measurements with the primary collimator;
2. Measurements with primary + intermediate collimator;
3. Measurements with primary + intermediate + cones.

According to Kilby et al. (2020) (5), the intermediate collimator has the same field size as the 60 mm cone, which was adopted as the reference field. Percent depth dose (PDD) curves were obtained with a SSD of 80 cm, and lateral dose profiles (LDP) with a source-to-axis distance (SAD) of 80 cm, following the methodology proposed by Aaraki (2006) (13). Measurements were performed for cones of 60, 40, 20, 10, and 5 mm (PDD) and, specifically for the 60 mm cone, LDP at depths of 10 cm and 20 cm. The detector used was the EDGE diode (Sun Nuclear), with an active volume of 0.8 × 0.8 × 0.03 mm³, suitable for high spatial resolution (14).

2.3. Computational Modeling

The computational modeling of the head is shown in Figure 3, including the photon source, primary collimator, intermediate collimator, and cones. The water phantom was positioned 80 cm from the source (SSD/SAD). Collimator dimensions were obtained using trigonometric relations and proportionality based on manufacturer technical drawings (10), while cones were measured using a caliper.

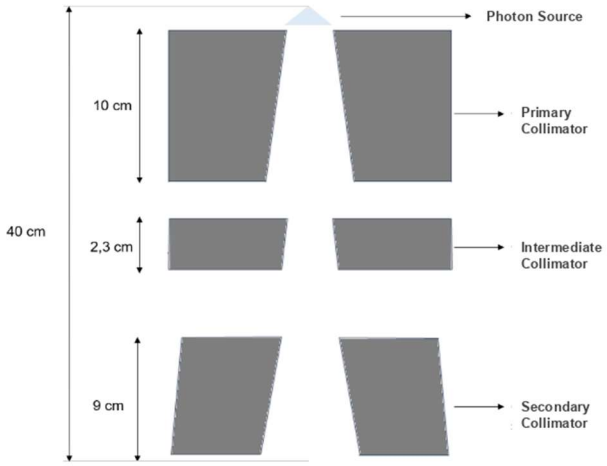

Figure 3. Schematic representation of collimator modeling: 2D view (left) and 3D view (right). Source: Author.

The source was modeled using a photon energy spectrum generated from a 60 mm IRIS™ phase-space (PhSp) provided by the IAEA (2011) (15), based on a 7 MeV electron beam with a Gaussian distribution of 0.23 cm over a 0.14 cm tungsten target (9). The validity of using this spectrum to simulate the flattening filter-free beam was confirmed by Souza et al. (2023) (16).

Different circular source sizes (1, 2, and 3 mm) were simulated to analyze the effect of focal spot size on dose distributions. Additionally, a 5° beam divergence was included to adjust the beam's angular opening and field size at the measurement distance. Simulated curves were obtained in three stages: first, the primary and intermediate collimators for geometric verification; then, PDD and LDP curves of the 60 mm cone as the basis for model adjustment.

Dose distributions were calculated in voxels of 2 × 2 × 1 mm³ to keep dimensions as close as possible to the EDGE detector size and reduce simulation uncertainty. The F8 tally from MCNP6 was used for energy-deposition calculations, in units of MeV. Specific parameters were defined to optimize simulations, including cutoff energies for electrons (ecut = 0.521 MeV) and photons (pcut = 0.01 MeV). Additionally, the variance-reduction technique Geometry Splitting/Russian Roulette was employed to improve simulation efficiency and minimize uncertainty, given that the voxels were of millimeter-scale.

Simulations were executed on a cluster with an Intel® Xeon® E5-2680 v4 processor (121 cores), 256 GB RAM, and storage on four 1 TB HDDs. The average simulation time was 15 hours, with 5 × 10^{10} primary photons.

2.4. Results Analysis

The theoretical analysis of small-field effects on the depth of maximum dose was based on the IAEA (2017) (8) criterion for reliable measurements, which establishes that the full width at half maximum (FWHM) of the radiation field relative to the minimum range of secondary electrons required to reach the electron equilibrium limit (r_{EEL}) and the largest dimension of the detector's active volume (d) must satisfy Equation (1):

$$FWHM = 2r_{EEL} + d \quad (1)$$

Model validation was based on the criteria established by IAEA Technical Report Series No. 430 (17), with relative difference limits presented in Table 1.

Table 1. Acceptable limits for the mean relative difference in different dose distribution regions.

Region	Tolerable Limit (≤)
Central axis (after buildup)	2%
Off-axis (profile center)	3%
Buildup and penumbra	10%
Umbra	30%

Source: (17).

PDD curves were evaluated in the buildup and post-buildup regions, while LDP curves were analyzed in the central axis, penumbra, and umbra regions.

3. Results and Discussion

3.1. Analysis of Clinical PDD Curves

Figure 4 illustrates the clinical PDD curves obtained for various collimators, from the primary collimator (115 × 110 mm) to the 5 mm cone. As the field size decreases, the position of the maximum dose (D_{max}) progressively moves closer to the surface (Table 2).

For the 60 mm cone (reference field), D_{max} occurs at a depth of 1.5 cm, whereas for the 5 mm cone, this depth is reduced to 1.0 cm, representing a relative difference of 33%. This variation demonstrates the dependence of dose distribution on field size, as discussed by Das et al. (2021) (7) and Khan & Gibbons (2014) (18).

In particularly small fields, the depth dose distribution is predominantly determined by the primary radiation, with the contribution of scattered photons minimized to the point of being negligible. In contrast, for larger fields, scattering contributes significantly to the absorbed dose due to the greater volume of tissue available for radiation dispersion (19).

As the field reaches dimensions sufficient to establish lateral electronic equilibrium (LEE) in the medium, the depth of maximum dose (D_{max}) tends to stabilize. This behavior was observed in fields 40 mm or larger. In narrow fields, where LEE is not achieved, there is a reduction in the number of secondary electrons contributing to the central-axis dose, resulting in a dose peak closer to the surface (18).

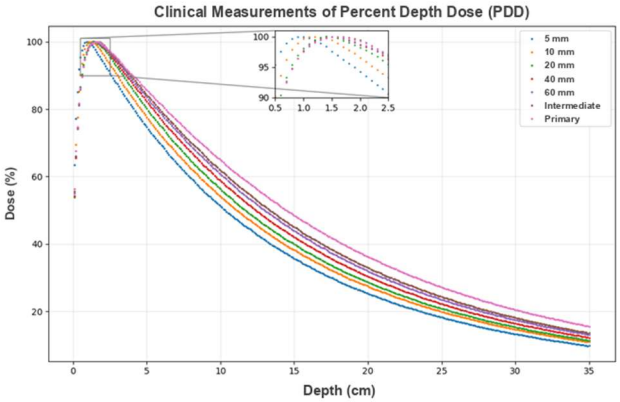

Figure 4. Clinical PDD curves for different field sizes, highlighting the D_{max} region for a clearer visualization of the effect of field size on depth. Source: Author.

Table 2. D_{max} depth for different collimators.

Collimator	Depth D_{max} (cm)
Primary (115 x 110 mm)	1.5
Intermediate (60 mm)	1.5
60 mm Cone	1.5
40 mm Cone	1.5
20 mm Cone	1.4
10 mm Cone	1.2
5 mm Cone	1.0

Source: Author (2026).

The results obtained are consistent with the relationship established in Equation (1). According to the TG-155 report, for 6 MV beams, the minimum range required to reach full LEE in water is 11 mm (7). Considering the largest dimension of the sensitive volume of the detector used in the measurements (0.8 mm), the minimum full width at half maximum

(FWHM) necessary to satisfy equilibrium conditions is approximately 22.8 mm. This discussion is supported by the observation that the depth of maximum dose begins to decrease for the 20 mm field.

3.2. Validation of the Computational Model

PDD and LDP curves for the 60 mm cone were evaluated considering sources with diameters of 1 mm, 2 mm, and 3 mm. According to Das et al. (2021) (7), the shape of the PDD curves remains practically unchanged across different source sizes when the field diameter is 5 mm or greater, with beam energy being the main factor shaping the central-axis dose distribution. However, as shown in Figure 5, the relative difference increases in the post-buildup region as the source diameter increases, possibly due to scattering effects and greater simulation uncertainty at larger depths.

Furthermore, the spatial distribution of the source significantly influences the lateral dose profile, as indicated by the TG-155 report (7).

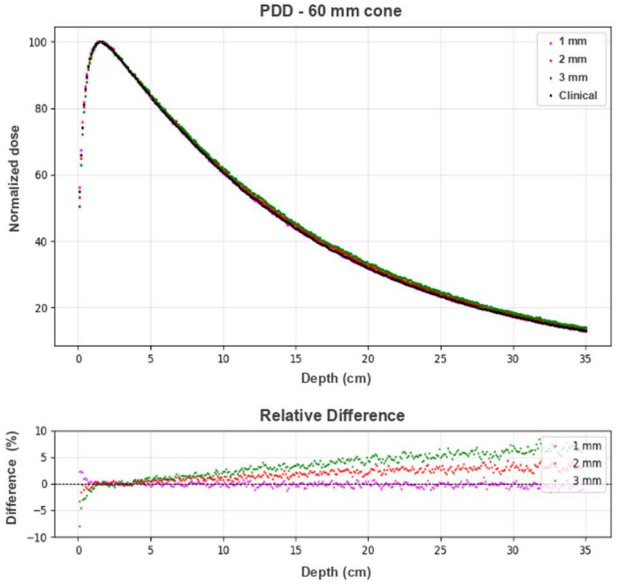

Figure 5. Depth dose distribution curve for the 60 mm cone compared to simulated models with source diameters of 1 mm, 2 mm, and 3 mm. Source: Author.

Furthermore, the spatial distribution of the source significantly influences the lateral dose profile, as indicated by the TG-155 report (7). The comparison between the different simulated source sizes and the clinical data obtained at depths of 10 cm (Figure 6) and 20 cm (Figure 7) shows visually noticeable differences, attributed to variations in source size and shape, as well as the lack of detailed technical information on the clinical equipment.

The mean relative differences between the clinical and simulated PDD and LDP curves in different regions are presented in Tables 3 and 4. It should be noted that, as discussed with the clinical team, reporting experimental uncertainties for this type of measurement is not a routine practice; therefore, only simulation-derived errors are presented.

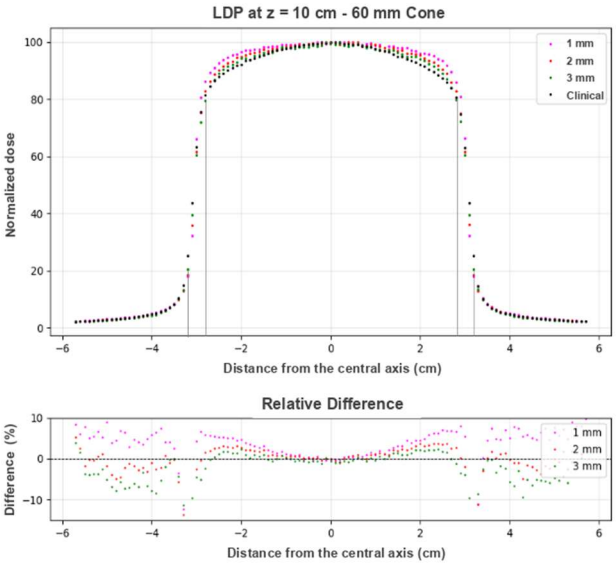

Figure 6. Lateral dose profile for the 60 mm cone compared to simulated models measured at 10 cm depth, with source diameters of 1 mm, 2 mm, and 3 mm. Source: Author.

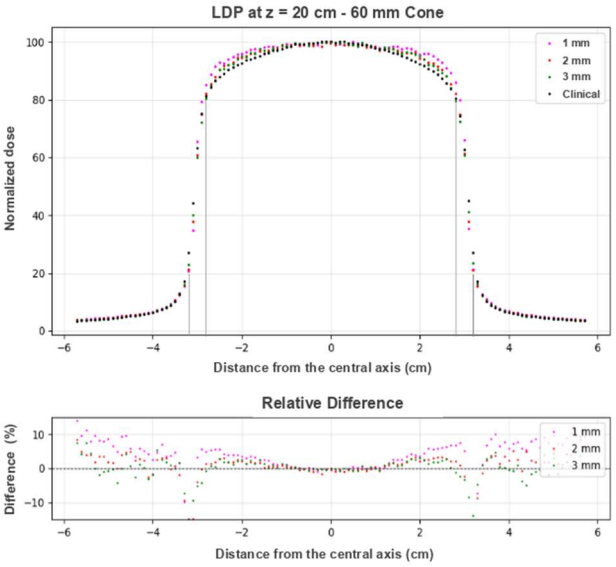

Figure 7. Lateral dose profile for the 60 mm cone compared to simulated models measured at 20 cm depth, with source diameters of 1 mm, 2 mm, and 3 mm. Source: Author.

Table 3. Relative difference in the PDD regions of the 60 mm cone.

Source (mm)	Buildup [10%]	Post-Buildup [2%]
1	0.78	0.34
2	0.70	2.00
3	1.94	3.87

Source: Author (2026).

The comparative analysis between clinical and simulated data reveals that, in the buildup region, all sources remained within the 10% tolerance limit. In the post-buildup region, only the 1 mm and 2 mm diameters complied with the 2% limit. For lateral profiles at depths of 10 cm and 20 cm, all diameters remained within the established criteria, with the 3 mm source showing the smallest relative difference at the profile center.

Table 4. Relative difference in the LDP regions of the 60 mm cone at depths of z = 10 cm and z = 20 cm.

Depth	Source (mm)	Center [3%]	Penumbra [10%]	Umba [30%]
10 cm	1	2.69	7.19	5.06
	2	1.55	8.80	1.40
	3	0.52	7.65	4.26
20 cm	1	2.19	5.55	6.35
	2	0.95	7.72	2.08
	3	0.90	6.36	0.53

Source: Author (2026).

However, when considering all evaluated regions simultaneously, including buildup, post-buildup, central axis, penumbra, and umbra, the 2 mm source demonstrated the best overall performance, remaining within tolerance limits in all cases. These results justify its selection as the ideal model for representing the CyberKnife® system source.

The literature highlights the complexity involved in determining the physical parameters of sources in radiotherapy systems, often limited by the lack of specifications provided by manufacturers. In many studies, a Gaussian spatial distribution is assumed for circular sources with diameters between 1 mm and 3 mm. However, the MCNP6 code presents limitations for accurately modeling Gaussian distributions in circular sources, a relevant consideration given the beam geometry produced by the CyberKnife® (7, 10).

Therefore, in this study, a circular source with a uniform distribution was adopted. This choice is supported by several investigations in the literature, such as the works of Francescon, Cora, and Cavedon (2008) (9), Duchaine, Markel, and Bouchard (2022) (20), and Wang et al. (2021) (21), which reported good reproduction of results using sources with Gaussian distributions close to 2 mm. Notably, Wang et al. (2021) (21) validated the use of a photon source with a radial Gaussian distribution by comparing it with models based on full electron beams, demonstrating that the photon source was able to accurately reproduce dose distributions, reducing complexity and computational time.

Thus, the results obtained in this study support the choice of a 2 mm diameter source as suitable for modeling the CyberKnife® system. This decision aligns with the evidence in the literature, reinforcing the robustness and applicability of the adopted model.

4. Conclusions

The results of this study demonstrate that modeling the CyberKnife® stereotactic radiosurgery system using the Monte Carlo method, implemented in the MCNP6 code is feasible and reliable, exhibiting strong agreement with experimental dosimetric data, particularly for the 60 mm cone. The simulation of PDD and LDP curves proved to be sensitive to the simulated source diameter, with the 2 mm model showing the best overall performance across all analyzed regions.

The accuracy of the modeling is particularly relevant for small-field dosimetry, where lateral electronic equilibrium is not achieved and conventional protocols face limitations. In such cases, Monte Carlo simulations are an essential tool for complementing and, in some situations, replacing clinical measurements, thereby enabling precise adjustment of treatment plans.

Although phase-space data for the fixed collimators of the CyberKnife® system are not yet available, the adopted strategy using a uniform source and parameters validated in previous studies proved to be both robust and effective. The use of finely discretized voxels further improved simulation accuracy, providing a reliable foundation for detector validation and the assessment of new clinical protocols.

From a broader perspective, this work provides a solid foundation for the continued advancement of computational modeling in radiotherapy, encouraging the exploration of alternative Monte Carlo codes or adaptations within MCNP6. The findings presented here can be extended to model other cone collimator sizes and secondary collimation systems, such as IRIS™ and MultiLeaf™. Thus, this study not only validates an efficient approach for CyberKnife® system modeling but also promotes further investigations comparing different platforms and varying source parameters, ultimately reinforcing the role of computational modeling as a key tool in high-precision treatment planning.

Acknowledgements

To the Nuclear and Energy Research Institute (IPEN) and the National Nuclear Energy Commission (CNEN) for the master's scholarship. To Hospital Vila Nova Star and its Medical Physics team for support in the experimental measurements.

References

1. Das, I. J.; Ding, G. X.; Ahnesjö, A. Small fields: nonequilibrium radiation dosimetry. Medical physics, Wiley Online Library, v. 35, n. 1, p. 206–215, 2008.
2. Trifiletti, D. M.; et al. Stereotactic radiosurgery and stereotactic body radiation therapy. Switzerland AG: Springer International Publishing, 2019.
3. Leksell, L. The stereotaxic method and radiosurgery of the brain. Acta chir scand, v. 102, p. 316–319, 1951.
4. Jr, J. R. A.; et al. Image-guided robotic radiosurgery. Neurosurgery, LWW, v. 44, n. 6, p. 1299–1306, 1999.
5. Kilby, W.; et al. A technical overview of the CyberKnife system. In: Handbook of robotic and image-guided surgery. Elsevier, p. 15–38, 2020.
6. Fransson, P.; et al. Ultra-hypofractionated versus conventionally fractionated radiotherapy for prostate cancer (Hypo-RT-PC): patient-reported quality-of-life outcomes of a randomised, controlled, non-inferiority, phase 3 trial. The Lancet Oncology, Elsevier, v. 22, n. 2, p. 235–245, 2021.
7. Das, I. J.; et al. Report of AAPM Task Group 155: Megavoltage photon beam dosimetry in small fields and non-equilibrium conditions. Medical physics, Wiley Online Library, v. 48, n. 10, p. e886–e921, 2021.
8. IAEA, T. 483. Dosimetry of small static fields used in external beam radiotherapy: an IAEA-AAPM International Code of Practice for reference and relative dose determination. [S.l.], 2017.
9. Francescon, P.; Cora, S.; Cavedon, C. Total scatter factors of small beams: a multidetector and Monte Carlo study. Medical physics, Wiley Online Library, v. 35, n. 2, p. 504–513, 2008.
10. Accuray Incorporated. CYBERKNIFE® TREATMENT DELIVERY SYSTEM: Technical Specifications. Sunnyvale, CA, 2018.
11. Lan, J.-H.; et al. Physical characteristics of fixed and dynamic collimator for CyberKnife M6. 2016 3rd International

Conference on Green Technology and Sustainable Development (GTSD), p. 1–4, 2016.
12. Sun Nuclear Corporation. SunSCAN™3D. s.d a. Disponível em: SunSCAN 3D: Next-Gen Cylindrical Water Scanning System - Sun Nuclear.
13. Araki, F. Monte Carlo study of a CyberKnife stereotactic radiosurgery system. Medical physics, Wiley Online Library, v. 33, n. 8, p. 2955–2963, 2006.
14. Sun Nuclear Corporation. EDGE Detector™. Melbourne, Flórida: Sede Corporativa, 3275 Suntree Boulevard, Estados Unidos: [s.n.], s.d.b. Disponível em: EDGE Detector™ - Sun Nuclear. Access: 05 fev 2023.
15. IAEA– International Atomic Energy Agency. Phase-space database for external beam radiotherapy: Photon PHSP data for CyberKnife with IRIS collimator. 2011. Available at: Index of /phsp/photon/CyberKnife_IRIS.
16. Souza, C. H.; et al. Análise da fluência de fótons de um feixe direto para construção de um modelo de fonte virtual de um acelerador linear clínico em Monte Carlo. In: XXVII CBFM: Congresso Brasileiro De Física Médica. São Pedro, SP: [s.n.], 2023.
17. IAEA. Commissioning and Quality Assurance of Computerized Planning Systems for Radiation Treatment of Cancer. [S.l.], 2004.
18. Khan, F. M.; Gibbons, J. P. Khan's The physics of radiation therapy. [S.l.]: Lippincott Williams & Wilkins, 2014.
19. Kastrati, L.; et al. Applications and benefits of using gradient percentage depth dose instead of percentage depth dose for electron and photon beams in radiotherapy. Polish Journal of Medical Physics and Engineering, v. 27, n. 1, p. 25–29, 2021.
20. Duchaine, J.; Markel, D.; Bouchard, H. A probabilistic approach for determining Monte Carlo beam source parameters: I. modeling of a CyberKnife M6 unit. Physics in Medicine & Biology, IOP Publishing, v. 67, n. 4, p. 045007, 2022.
21. Wang, J.; et al. An automated optimization strategy to design collimator geometry for small field radiation therapy systems. Physics in Medicine & Biology, IOP Publishing, v. 66, n. 7, p. 075016, 2021.

Contact:

Aline Aparecida da Costa Granja
FICSAE - Faculdade Israelita de Ciências da Saúde Albert Einstein, Hospital Albert Einstein
Av. Prof. Francisco Morato, 4293 - Butantã, São Paulo - SP, 05521-200
alineacgranja@gmail.com